

Supporting Information for

Defect-Tolerant Plasmonic Elliptical Resonators for Long-Range Energy Transfer

Felipe V. Antolinez,[†] Jan M. Winkler,[†] Patrik Rohner,[‡] Stephan J. P. Kress,[†] Robert C. Keitel,[†] David K. Kim,[†] Patricia Marqués-Gallego,[†] Jian Cui,^{†,§} Freddy T. Rabouw,^{†,§} Dimos Poulikakos[‡] and David J. Norris^{,†}*

[†]Optical Materials Engineering Laboratory, Department of Mechanical and Process Engineering,
ETH Zurich, 8092 Zurich, Switzerland

[‡]Laboratory of Thermodynamics in Emerging Technologies, Department of Mechanical and Process Engineering,
ETH Zurich, 8092 Zurich, Switzerland

^{*}Corresponding author. E-mail: dnorris@ethz.ch

S1. Sample Fabrication

Materials. Two- or four-inch diameter, single-side-polished, single-crystalline Si(100) wafers with <0.4 nm root-mean-square (RMS) roughness and thicknesses of 1000 μm were purchased from Silicon Valley Microelectronics or Silicon Quest. Four-inch wafers were diced into $2 \times 2 \text{ cm}^2$ or $1.5 \times 1.5 \text{ cm}^2$ square pieces. Sulfuric acid (H_2SO_4 , 95–98%, 258105) was purchased from Sigma. Hydrogen peroxide (H_2O_2 , 30%, AnalaR Normapur) was bought from VWR. Nitric Acid (65% HNO_3) was acquired from Fisher Chemical. 18.2 $\text{M}\Omega$ deionized water (DI) was obtained from a MilliQ Advantage A10 water-purification system. Silver (Ag, 99.999%) pellets were purchased from Kurt Lesker. Tungsten dimple boats ($49 \times 12 \times 0.4 \text{ mm}^3$) were bought from Umicore. Acetone (Technic France, Micropur VLSI Grade), isopropanol (IPA, Technic France, Micropur VLSI Grade), CSAR 62 resist (AR-P 6200.04 and AR-P 6200.09, Allresist GmbH), developer for CSAR 62 resist (AR 600-546, Allresist GmbH), and buffered

oxide etch (BOE, hydrogen fluoride : ammonium fluoride 1:7, Technic France, Micropur VLSI Grade) were provided by the Binnig and Rohrer Nanotechnology Center (BRNC) at IBM Zurich.

Fabrication of plasmonic ellipse templates. Plasmonic elliptical resonator structures were fabricated using template stripping.^{S1} Templates containing scattering Ag disks require a two-step electron-beam process. In the first step, $2 \times 2 \text{ cm}^2$ Si(100) chips containing negative electron-beam alignment marks were first cleaned using acetone, isopropanol, and O₂ plasma (PVA-TePla, GIGAbatch 310M, 600 W, 5 min). After a prebake (hotplate, 180 °C, 10 min), the chips were coated with a 127-nm-thick layer of AR-P 6200.04 (spin coater, 2000 rpm) and then soft-baked (hotplate, 150 °C, 5 min). Disks with 200 nm diameter, finally serving as scatterers, were defined using electron-beam (e-beam) lithography (Vistec, NFL 5) and then developed in AR 600-546 for 1 min followed by rinsing in isopropanol and drying with a N₂ gun. Approximately 100 nm deep holes were etched into the Si chips using HBr-based inductive coupled plasma etch (Oxford Instruments, PlasmaPro 100 Cobra, 80 W) for 35 s. The resist was removed by sonication in acetone and isopropanol for 2 min each, followed by O₂ plasma ashing (PVA TePla, GIGAbatch 310M, 600 W, 5 min). After dipping in BOE, the chip was cleaned for 10 min in piranha solution (1:1 mixture of H₂SO₄ and H₂O₂; caution: this solution reacts violently with solvents and other organic material). In a final step, the chip was thoroughly rinsed in DI water and then dried with a N₂ gun.

The elliptically shaped block reflectors were fabricated in a second e-beam lithography run. After following the same protocol for cleaning as above, the chips were coated with a 284 nm thick layer of AR-P 6200.09 (spin coater, 2000 rpm). Elliptical annuli of 2 μm width were defined using e-beam lithography. Before cleaning the chip, approximately 600 nm deep trenches were etched into the Si chips using HBr-based inductive coupled plasma etch (Oxford Instruments, PlasmaPro 100 Cobra, 80 W) for 2 min 30 s. If only reflectors were desired, the first lithography run was left out and thus e-beam markers became redundant.

Deposition of Ag films and template stripping. A thermal evaporator (Kurt J. Lesker, Nano36) was used for the Ag-film deposition. Deposition of a 1 μm thick Ag film onto the ellipse templates mounted

on a tilt-rotate stage was performed with Ag pellets evaporated from a tungsten dimple boat at high rates ($>25 \text{ \AA s}^{-1}$) and low residual gas pressures ($3\times10^{-7} \text{ mbar}$).^{S2} The deposited Ag film was template-stripped by bonding a microscope slide to the film using an ultraviolet-light-curable epoxy (EpoTek, OG142-95). The Ag-epoxy-glass stack was then stripped from the template to reveal elliptical resonators. Ellipse templates can be reused by first removing the remaining Ag with nitric acid (HNO_3 , 10 min), then rinsing the templates in DI water, sonicating them in isopropanol for 5 min, and finally drying them with a N_2 gun.

Quantum-dot inks for printing. For electrohydrodynamic nanodripping, we used two inks based on green and red quantum dots (QDs), respectively. The green CdSe/ZnS core/shell QDs (~10 nm particle diameter) with a compositionally graded shell emit at ~550 nm and were synthesized according to a protocol described in the Supporting Information of Prins *et al.*^{S3} The red CdSe/CdS/ZnS core/shell QDs (~4.1 nm core diameter) emitting at ~630 nm were synthesized according to a protocol described in the Supporting Information of Kress *et al.*^{S4} The concentrations of the CdSe/ZnS and CdSe/CdS/ZnS core/shell dispersions in hexane were adjusted to an optical density (OD) of 6 and 2, respectively [measured at the lowest energy exciton peak in a ultraviolet-visible spectrometer (UV-VIS), using a quartz cuvette with a 1 mm path length]. Hexane was then replaced by tetradecane as the solvent of the QD dispersion by adding a volume equivalent of tetradecane to the dispersion and then storing it at room temperature overnight in an open glass vial to allow slow evaporation of the volatile hexane. The quantum-dot dispersion was subsequently passed through a $0.2 \mu\text{m}$ polytetrafluoroethylene (PTFE) membrane syringe filter. Prior to printing, the green CdSe/ZnS QD ink was diluted to a final concentration of OD 2 and the red CdSe/CdS/ZnS QD ink to a concentration of OD 0.5.

Electrohydrodynamic nanodripping of quantum dots (QDs). A detailed description of the electrohydrodynamic nanodripping setup^{S5} and a detailed study on printing colloidal QDs on plasmonic substrates can be found elsewhere.^{S6} In brief, a voltage is applied to a metal-coated nozzle to eject sub-attoliter ink droplets on demand. Nozzles for printing were fabricated by first pulling glass capillaries

(TW100-4, World Precision Instruments) using a Sutter Instruments P-97 pipette puller followed by coating with a 3-nm titanium adhesion layer and a 30-nm gold layer (electron-beam evaporation, Plassys, MEB550S). The outer diameter of the nozzles ranged between 0.9 and 1.4 μm . The plasmonic substrate was placed around 5 μm below the nozzle tip and horizontally positioned with a high-precision crossed-roller bearing stage (Aerotech ANT130-060-ULTRA). A 50 \times objective [Edmund Optics, Plan Apo ULWD; numerical aperture (NA), 0.42; working distance, 20.5 mm; tilt mount under 45°] was used for live monitoring and optical alignment of the printing process. A direct current (DC) electric potential of ~220 V was applied between the metal-coated nozzle (+) and the template-stripped silver substrate (ground) to eject ink. Each ensemble of QDs was printed by applying a voltage pulse for 120 ms.

S2. Optical Measurements

SPP excitation with a linearly polarized laser beam. SPPs at a Ag/air interface can be excited by focusing a laser beam onto a Ag disk, which scatters free-space photons into plasmons. Figure S1a shows a scanning electron micrograph of a template-stripped Ag substrate containing a Ag disk surrounded by a shallow Ag semi-circle (~100 nm height). Figure S1b,c shows the signal scattered from the shallow semi-circle when the Ag disk is excited with a horizontally or a vertically polarized HeNe laser beam, respectively. When the laser is linearly polarized, SPPs are launched predominantly in the polarization direction due to the longitudinal electric-field component of the transverse-magnetic SPP mode.^{S7} In contrast, photons would be scattered orthogonally to the polarization direction of the laser due to their transverse-electric nature. These results demonstrate that the measured signal indeed originates from SPP scattering and not from scattering of photons grazing over the interface. In the main text, SPPs are excited with a radially polarized laser beam to ensure omnidirectional launching of plasmons.

SPP excitation with a super-continuum laser beam. To probe the eigenmode spectrum supported by our particular resonator, we utilized broadband light generated from a sapphire crystal and a 1040 nm pulsed laser. The resulting super-continuum pulses were focused onto the Ag disk at F₁, launching broadband SPPs into the resonator. Spectra were then collected for those SPPs that were scattered at the

second Ag disk at F_2 using an imaging spectrograph. Figure S4a shows the experimental transmission spectrum of an elliptical resonator. The blue line shows the same data as in Figure 2a of the main text, the red line depicts the same transmission spectrum normalized by the spectrum of the super-continuum source reflected off a Ag surface (black dotted line). Because of chromatic aberrations, both the reflection spectrum from a flat Ag surface and the SPP-in-coupling spectrum on a Ag disk depend sensitively on the objective–surface distance. Therefore, the reflection spectrum used for normalization here (dashed line) has only approximately the same shape as the excitation spectrum at the Ag disk at F_1 . We measured the reflection spectrum by focusing the super-continuum source on a flat Ag surface and adjusting the sample height such that the reflected spot produced the smallest possible image on a camera. By closing the slit before the spectrograph and integrating only over a few pixel rows, the spectrum (black dotted line) was collected from a diffraction-limited area in the center of the focus.

S3. Modeling

Modeling the transmission spectrum of a plasmonic ellipse. Figure S4a shows the experimental transmission spectrum of an elliptical resonator (same data as in Figure 2a of the main text). To calculate the transmission spectrum of our ellipse, we use a plasmonic Fabry–Pérot model that is based on the accumulated phase per round trip in a resonator.⁸⁸ In our case, every ray leaving one focal point of the ellipse will arrive at the other focal point after one reflection. Consequently, after two reflections, every ray will return to the focal point from where it originated. The length of a full round trip in the resonator is $d = 4a$, independent of the emission angle of the initial ray.

Interfering the complex electric fields after infinitely many round trips in the elliptical resonator results in an SPP intensity of

$$I_{\text{FP}}(\lambda) = \frac{1}{|1 - r(\lambda)^2 e^{-ik_{\text{SPP}}d}|^2}.$$

Here, the wave amplitude is attenuated by the imaginary part of k_{SPP} and the finite reflectivity of the resonator wall. We estimate the reflection at the wall using a Fresnel-type equation, in which the reflectivity depends on the wavelength λ and the incidence angle θ

$$r(\lambda, \theta) = \frac{\sqrt{k_{\text{SPP}}^2 - k_{\text{SPP}}^2 \sin(\theta)^2} - \sqrt{\varepsilon_m k_0^2 - k_{\text{SPP}}^2 \sin(\theta)^2}}{\sqrt{k_{\text{SPP}}^2 - k_{\text{SPP}}^2 \sin(\theta)^2} + \sqrt{\varepsilon_m k_0^2 - k_{\text{SPP}}^2 \sin(\theta)^2}} \quad (\text{S1})$$

where $k_{\text{SPP}} = k_0 \sqrt{\frac{\varepsilon_m \varepsilon_d}{\varepsilon_m + \varepsilon_d}}$ is the SPP dispersion relation. The free-space wave vector is $k_0 = 2\pi/\lambda$, and $\varepsilon_d = 1$ and ε_m are the relative permittivities of air and template-stripped Ag, respectively.^{S2} However, the Fabry–Pérot model cannot accommodate a reflection coefficient that is different for every round trip. Therefore, we approximate the complex reflectivity $r(\lambda, \theta)$ by the reflectivity at normal incidence ($\theta = 0$). This approximation is justified because after a few round trips, the rays are propagating along paths that are nearly parallel to the long axis of the ellipse and therefore always reflecting close to normal incidence.

Figure S4b shows the normalized ellipse transmission spectrum calculated with the plasmonic Fabry–Pérot model. As expected for the dispersive SPP mode, the resonance peak spacing is not constant, but a function of the wavelength. Due to the lower plasmon loss at longer wavelengths, the resonance amplitude increases and the linewidth decreases with increasing wavelength. Our plasmonic Fabry–Pérot model correctly predicts the approximate spacing of the resonance peaks observed in Figure S4a. However, a modulation in the resonance amplitude is observed in the experiment that is not captured by the plasmonic Fabry–Pérot model.

We used COMSOL Multiphysics to simulate the ellipse transmission spectrum using the finite-element method in the frequency domain. Since the predominant electric field component of SPPs is the component normal to the interface, the plasmonic ellipse was approximated as a two-dimensional

structure. It was modeled as an ellipse with the complex mode index for SPPs at a Ag–air interface $n_{\text{SPP}} = \sqrt{\frac{\epsilon_m \epsilon_d}{\epsilon_m + \epsilon_d}}$, surrounded by silver with permittivity ϵ_m .

To calculate the transmission spectrum in Figure S4c, a dipole source perpendicular to the surface was placed at focal point F_1 , and the electric field intensity normal to the surface was evaluated at the other focal point, F_2 . The resulting transmission spectrum shows multiple sets of resonances, each of which exhibits an intensity modulated by an envelope function. This numerical model captures the experimentally observed resonance intensity modulation in the data well, considering that the exact shape of the intensity modulation is sensitive to the exact location of the dipole source. Figure S4d shows the simulated spectrum when the dipole is shifted 100 nm from the focus. This indicates that small discrepancies in the placement of the Ag disks can explain the spectral shift observed between experiment (Figure S4a) and our simulation (Figure S4c).

The plasmonic Fabry–Pérot model is less accurate in predicting the observed transmission spectrum for two reasons. First, the model cannot include the angle-dependent reflectivity which results in varying phase differences for each round trip in the ellipse. Second, the ray-like interference model cannot take into account the diffraction limit. The physical reason for the intensity modulation in the COMSOL model is that the electric field hotspots of the resonances move slightly away from the focal points and thus the coupling of the dipole varies as a function of the wavelength.

Modeling the spatial intensity distribution inside a plasmonic ellipse. A simple analytical interference model for SPPs can provide physical insight into the scattered intensity modulation along the elliptical reflector (Figure S3a) and thus the spatial intensity distribution of an ellipse eigenmode. When the Ag disk at focal point F_1 is excited with a focused radially polarized laser beam, the SPPs propagating away from the source can be modeled as an isotropic circular wave that decays exponentially as a function of the propagation distance. Since the electric field of SPPs is polarized predominantly in the direction

normal to the interface, the longitudinal field component of the plasmon can be neglected. The out-of-plane electric field decays as

$$E(d) \propto \sqrt{\frac{1}{k_{\text{SPP}} d}} e^{ik_{\text{SPP}} d}$$

where $k_{\text{SPP}} = k_0 \sqrt{\frac{\epsilon_m \epsilon_d}{\epsilon_m + \epsilon_d}}$ is the dispersion relation for SPPs, and d the distance from the source. The free-space wave vector is $k_0 = 2\pi/\lambda$, and $\epsilon_d = 1$ and ϵ_m are the relative permittivities of air and template-stripped Ag, respectively.^{S2} The prefactor to the exponential ensures that the intensity integrated over all in-plane angles decays as $I(d) = |E|^2 \propto \frac{1}{d}$.

To first order, the electric field at a point P along the reflector can be calculated as a superposition of two paths (see Figure S3a): (1) the electric field E_1 from the direct path $|PF_1| = c$ (blue arrow), and (2) the electric field E_2 after one reflection and going through the focal point F_2 (green arrow).

$$E_P = E_1 + E_2 = \sqrt{\frac{1}{k_{\text{SPP}} c}} e^{ik_{\text{SPP}} c} + r(\theta_2) \sqrt{\frac{1}{k_{\text{SPP}}(2a-c)}} e^{ik_{\text{SPP}}(4a-c)} \quad (\text{S2})$$

The angle-dependent reflectivity is modeled as described above (eq. S1).

The intensity scattered out at point P is:

$$I_{\text{scat}} \propto (1 - |r(\theta_1)|^2) |E_P|^2$$

where $|E_P|^2$ is the electric field intensity at point P and $(1 - |r(\theta_1)|^2)$ takes into account the angle-dependent scattering efficiency (assuming that all the SPPs that are not reflected are scattered).

The calculated scattered intensity distribution in Figure S3a is very similar to the experiment shown in Figure 2c of the main text. Differences in the complex Ag permittivity or the exact size of the ellipse could explain the deviation between the modeled and experimental intensity modulation at the reflector.

Rate-equation model for energy transfer. We set up a rate-equation model to quantify the contribution of energy transfer to the total acceptor fluorescence emission signal from time-resolved measurements.

First, we fit the instrument response function of the system to the convolution of a Gaussian function with an exponential decay (exponentially modified Gaussian function)

$$P(t) = P_0 \exp \left[\frac{\gamma}{2} (2t_0 + \gamma\sigma^2 - 2t) \right] \operatorname{erfc} \left[\frac{t_0 + \gamma\sigma^2 - t}{\sqrt{2}\sigma} \right]. \quad (\text{S3})$$

The optimal fit parameters are shown in Table S1. The values of σ , the width of the Gaussian function, and γ , the decay of the exponential component, were fixed for all further fits to the photoluminescence decay curves of the quantum dots.

Second, we constructed a model for the photon count rate $\phi_i(t)$ from our donor and acceptor quantum dots upon direct excitation using a rate-equation model. To capture the multi-exponential decay dynamics, we considered two subpopulations ($j = 1, 2$) with different lifetimes for both the donor and the acceptor quantum dots ($i = D, A$).

$$\frac{dN_1^i(t)}{dt} = \alpha_1^i P(t) - \frac{N_1^i(t)}{\tau_1^i} \quad (\text{S4})$$

$$\frac{dN_2^i(t)}{dt} = \alpha_2^i P(t) - \frac{N_2^i(t)}{\tau_2^i} \quad (\text{S5})$$

$$\phi_i(t) = N_1^i(t) + N_2^i(t) + c^i \quad (\text{S6})$$

Here, $N_1^i(t)$ and $N_2^i(t)$ are the number of excited emitters in the two populations as a function of time. The fitting parameters α_1^i and α_2^i denote the number of emitters in the two populations, τ_1^i and τ_2^i are the lifetime of the two populations, and c^i is the background count rate in the measurement. The resulting values are shown in Table S2 for the donor and in Table S3 for the acceptor. The values of parameters α_1^i , α_2^i , τ_1^i , and τ_2^i are fixed in the fit of the overall energy-transfer model below.

To model the energy-transfer process, where the donor (green) quantum dots are excited and emission from the acceptor (red) quantum dots is detected, we used the following set of four coupled rate equations:

$$\frac{dN_1^D(t)}{dt} = \alpha_1^D P(t) - \frac{N_1^D(t)}{\tau_1^D} \quad (\text{S7})$$

$$\frac{dN_2^D(t)}{dt} = \alpha_2^D P(t) - \frac{N_2^D(t)}{\tau_2^D} \quad (\text{S8})$$

$$\frac{dN_1^A(t)}{dt} = \mu_P \alpha_1^A P(t) + \mu_{ET} \left[\alpha_1^A \alpha_1^D \frac{N_1^D(t)}{\tau_1^D} + \alpha_1^A \alpha_2^D \frac{N_2^D(t)}{\tau_2^D} \right] - \frac{N_1^A(t)}{\tau_1^A} \quad (S9)$$

$$\frac{dN_2^A(t)}{dt} = \mu_P \alpha_2^A P(t) + \mu_{ET} \left[\alpha_2^A \alpha_1^D \frac{N_1^D(t)}{\tau_1^D} + \alpha_2^A \alpha_2^D \frac{N_2^D(t)}{\tau_2^D} \right] - \frac{N_2^A(t)}{\tau_2^A} \quad (S10)$$

and

$$\phi_{ET}(t) = N_1^A(t) + N_2^A(t) + c \quad (S11)$$

for the photoluminescence decay curve. This model was fitted to the data in Figure 4f of the main text, using only the efficiency μ_P of direct excitation of the acceptor by the pump and the efficiency μ_{ET} of donor–acceptor coupling as adjustable fit parameters. The value of the background count rate $c = 0.203$ was extracted as the mean of the decay trace before the pump pulse arrived and remained unchanged in the fit. The optimal fit parameters are shown in Table S4.

Figure S8 shows the resulting dynamics of the rate equation model with no direct 405-nm plasmon excitation ($\mu_P = 0$) and without contribution from energy transfer ($\mu_{ET} = 0$). The fact that the measured data (gray points) does not coincide with the curve for $\mu_{ET} = 0$ (black dashed line) is further proof that energy transfer significantly contributes to the acceptor-QD signal. To quantify the contribution of energy transfer to the decay signal, we calculated the integrated photon count rate of the rate-equation model with $\mu_P = 0$ and divided this number by the integrated photon count rate for the full model. We estimated that the contribution of the energy transfer was 34%.

S4. Direct Excitation of Red Acceptor QDs Through 405-nm SPPs

Contribution of direct laser excitation to energy transfer in elliptical resonators of different sizes.

When a 405-nm excitation laser is focused onto the green donor QDs, SPPs with different wavelengths are launched: green SPPs emitted by the QDs and 405-nm SPPs that are excited through scattering by the QDs. Due to the broad absorption spectrum of the red acceptor QDs, both wavelengths are absorbed and eventually re-emitted as photons. By only detecting the emitted red photons, it is not possible to determine the relative contributions of blue and green SPPs to the excitation of the acceptor QDs. In the main text, we address this challenge using a photokinetic analysis. Here, we validate these results by intentionally

photobleaching the green donor QDs, which experimentally eliminates one of the two excitation pathways.

We first excite the green donor QDs with a weak 405-nm laser and spectrally resolve the signal detected at the location of the acceptor QDs. Then, we increase the laser power to permanently photobleach the green QDs while still retaining this ensemble of particles to scatter photons. Finally, we decrease the laser power to the initial, low value and remeasure the spectrally resolved emission from the red QDs again.

The blue lines in Figure S6a,b show the spectra collected at the red acceptor QDs when the undamaged green donor QDs were excited, for elliptical resonators with $2e = 5 \mu\text{m}$, $2a = 8 \mu\text{m}$ and $2e = 15 \mu\text{m}$, $2a = 24 \mu\text{m}$, respectively. As in the data presented in Figure 4b in the main text, the peak centered at $\sim 550 \text{ nm}$ corresponds to SPPs launched by the donor QDs that are scattered into green photons at the acceptor. The second peak at $\sim 630 \text{ nm}$ results from photons emitted by red acceptor QDs following absorption of either a blue or a green SPP. The red lines in Figure S6a,b show the signal collected at the red acceptor QDs after photobleaching the green QDs. Now, no green scattering signal at 550 nm is visible, and we can assume that the acceptor QDs are solely excited through blue SPPs. The red QD-emission peak centered at $\sim 630 \text{ nm}$ is still observed, confirming that energy transfer mediated by 405-nm SPPs is present. However, the intensity of the red signal is weaker after photobleaching the donor QDs because green SPPs no longer contribute to the excitation of the acceptor. Comparing Figure S6a,b it becomes apparent that the remaining acceptor-emission intensity upon photobleaching (comparing blue and red lines) is smaller for larger values of $2a$. This suggests that the remaining intensity is due to excitation by 405-nm SPPs. Indeed, our results are consistent with the wavelength-dependent propagation losses of SPPs. As short-wavelength SPPs have shorter propagation lengths, the relative contribution of blue SPPs to the excitation of the acceptor QDs decreases for larger resonators. We quantify the contribution of 405-nm SPPs to the red emission intensity by taking the ratio between the red and blue spectra between 625 and 650 nm. For the $2e = 5 \mu\text{m}$ and $2e = 15 \mu\text{m}$ elliptical resonators, we obtain values of 0.85 and 0.23, respectively. As a comparison: based on the photokinetic analysis on an ellipse

with $2e = 10 \mu\text{m}$ presented in the main text, 0.66 of the red emission would be due to excitation through 405-nm SPPs.

Modeling the contribution of direct laser excitation to energy transfer in elliptical resonators of different sizes. We introduce a simple model that describes the resonator-size-dependent contribution of blue and green SPPs to the excitation of the red acceptor QDs. According to Figure S9a, we separate the emission intensity of the acceptor QDs into two parts: A contribution resulting from excitation through blue SPPs, I_R^{405} , and green SPPs, I_R^{550} , respectively:

$$I_R^{405} = I_0 \eta_{P \rightarrow SPP}^{405} r e^{-\frac{2a}{L_{SPP}^{405}} \eta_{SPP \rightarrow P}^{405}} \quad (\text{S12})$$

$$I_R^{550} = I_0 \eta_{P \rightarrow SPP}^{550} r e^{-\frac{2a}{L_{SPP}^{550}} \eta_{SPP \rightarrow P}^{550}} \quad (\text{S13})$$

where I_0 is the intensity of the excitation laser and $\eta_{P \rightarrow SPP}^{405}, \eta_{P \rightarrow SPP}^{550}$ are the probabilities that a blue photon excites a blue and green SPP, respectively. The exponential term considers the wavelength-dependent SPP damping where $2a$ is the distance between the focal points *via* one reflection and L_{SPP}^λ is the propagation length of an SPP with free-space wavelength λ , estimated based on ellipsometry data.^{S2} The reflectivity of the reflector is denoted as r and $\eta_{SPP \rightarrow P}^{405}, \eta_{SPP \rightarrow P}^{550}$ are the probabilities that a red photon is emitted upon arrival of a blue or green SPP at the acceptor, respectively. The intensity ratio of the red emission intensity before and after photobleaching of the donor QDs is given by:

$$\frac{I_R^{405}}{I_R^{405} + I_R^{550}} = \frac{1}{1 + \phi \exp\left(2a \frac{L_{SPP}^{550} - L_{SPP}^{405}}{L_{SPP}^{405} L_{SPP}^{550}}\right)} \quad \text{with } \phi = \frac{\eta_{P \rightarrow SPP}^{550} \eta_{SPP \rightarrow P}^{550}}{\eta_{P \rightarrow SPP}^{405} \eta_{SPP \rightarrow P}^{405}}. \quad (\text{S14})$$

Hence, ϕ describes the ratio of photon–SPP coupling strengths, mediated by the QDs, at 405 and 550 nm. Figure S9b plots the intensity ratio described in eq. S14 as a function of propagation distance $2a$ for different values of ϕ . As expected, the contribution of 405-nm SPPs decreases for larger resonators. For $\phi \approx 1$, the contribution of green excitation to the red emission is large even in small ellipses. For smaller ϕ , green SPPs make a significant contribution to the excitation of the acceptor only for large ellipses. The ratios extracted from the photobleaching experiments (Figure S9b) are shown as black circles. By fitting

eq. S14 to the data, we estimate that $\phi = 0.05$. We intentionally did not measure a data point for the $2e = 10 \mu\text{m}$ elliptical resonator as photobleaching would have irreversibly destroyed the sample. However, using $\phi = 0.05$, the model predicts an intensity ratio of 0.55 for the ellipse design studied in Figure 1 of the main text ($2e = 10 \mu\text{m}$, $2a = 16 \mu\text{m}$). This is in rather good agreement with the photokinetic analysis presented in Figure 4f of the main text, from which we extracted a value of 0.66.

S5. Supplementary References

- (S1) Nagpal, P.; Lindquist, N. C.; Oh, S. H.; Norris, D. J. Ultrasmooth Patterned Metals for Plasmonics and Metamaterials. *Science* **2009**, *325*, 594–597.
- (S2) McPeak, K. M.; Jayanti, S. V.; Kress, S. J. P.; Meyer, S.; Iotti, S.; Rossinelli, A.; Norris, D. J. Plasmonic Films Can Easily Be Better: Rules and Recipes. *ACS Photonics* **2015**, *2*, 326–333.
- (S3) Prins, F.; Kim, D. K.; Cui, J.; De Leo, E.; Spiegel, L. L.; McPeak, K. M.; Norris, D. J. Direct Patterning of Colloidal Quantum-Dot Thin Films for Enhanced and Spectrally Selective Out-Coupling of Emission. *Nano Lett.* **2017**, *17*, 1319–1325.
- (S4) Kress, S. J. P.; Antolinez, F. V.; Richner, P.; Jayanti, S. V.; Kim, D. K.; Prins, F.; Riedinger, A.; Fischer, M. P. C.; Meyer, S.; McPeak, K. M.; Poulikakos, D.; Norris, D. J. Wedge Waveguides and Resonators for Quantum Plasmonics. *Nano Lett.* **2015**, *15*, 6267–6275.
- (S5) Galliker, P.; Schneider, J.; Eghlidi, H.; Kress, S.; Sandoghdar, V.; Poulikakos, D. Direct Printing of Nanostructures by Electrostatic Autofocussing of Ink Nanodroplets. *Nat. Commun.* **2012**, *3*, 890.
- (S6) Kress, S. J. P.; Richner, P.; Jayanti, S. V.; Galliker, P.; Kim, D. K.; Poulikakos, D.; Norris, D. J. Near-Field Light Design with Colloidal Quantum Dots for Photonics and Plasmonics. *Nano Lett.* **2014**, *14*, 5827–5833.
- (S7) Drezet, A.; Stepanov, A. L.; Ditzbacher, H.; Hohenau, A.; Steinberger, B.; Ausseneegg, F. R.; Leitner, A.; Krenn, J. R. Surface Plasmon Propagation in an Elliptical Corral. *Appl. Phys. Lett.* **2005**, *86*, 1–3.
- (S8) Saleh, B. E. A.; Teich, M. C. *Fundamentals of Photonics*; Wiley: New York, NY, 1991; pp. 254–257.

S6. Supplementary Tables

Parameter	P_0	γ	σ	t_0
Optimal value	1.031	3.831 ns ⁻¹	0.108 ns	0.414 ns

Table S1. Resulting parameter values of the fit of the exponentially modified Gaussian function to the instrument response function.

Parameter	τ_1^D	τ_2^D	α_1^D	α_2^D	t_0	c^D
Optimal value	2.046 ns	9.449 ns	1.458	0.895	0.143 ns	1.068×10^{-3}

Table S2. Resulting parameter values of the fit of the donor rate-equation model to the decay trace of the donor QDs.

Parameter	τ_1^A	τ_2^A	α_1^A	α_2^A	t_0	c^A
Optimal value	2.535 ns	6.194 ns	1.535	0.811	0.204 ns	1.254×10^{-4}

Table S3. Resulting parameter values of the fit of the acceptor rate-equation model to the decay trace of the acceptor QDs.

Parameter	μ_P	μ_{ET}	t_0
Optimal value	0.835	0.147	0.239 ns

Table S4. Resulting parameter values of the fit of the acceptor rate-equation model to the decay trace of the acceptor QDs.

S7. Supplementary Figures

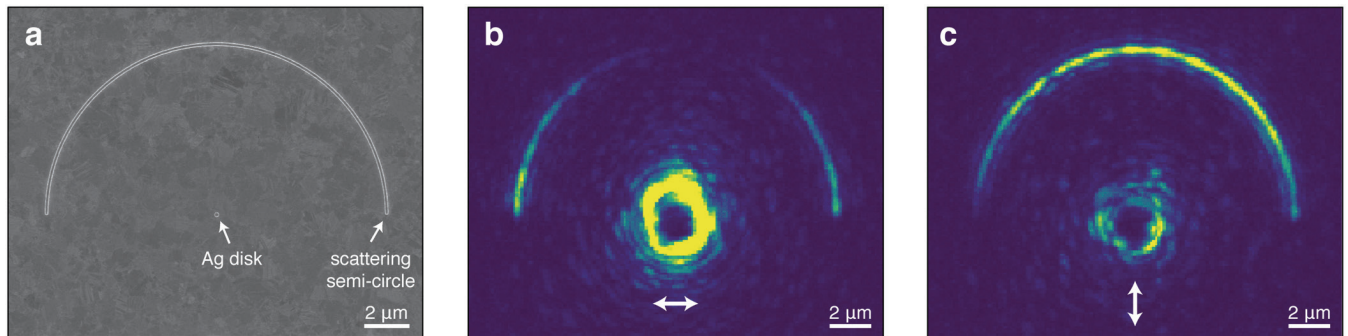


Figure S1. SPP excitation with a linearly polarized laser beam. (a) Scanning electron micrograph of a Ag disk for SPP excitation, surrounded by a shallow Ag semi-circle for SPP out-scattering. (b) Experimental intensity profile of scattering SPPs along the Ag semi-circle when the Ag disk is excited with a horizontally polarized HeNe laser (the white arrow indicates the polarization of the excitation laser in the center of the focus; no particular polarization is selected in the detection path). (c) SPP scattering along the Ag semi-circle when the Ag disk is excited with vertical polarization. These measurements demonstrate that the scattered signal originates from SPPs and not from photons grazing the interface.

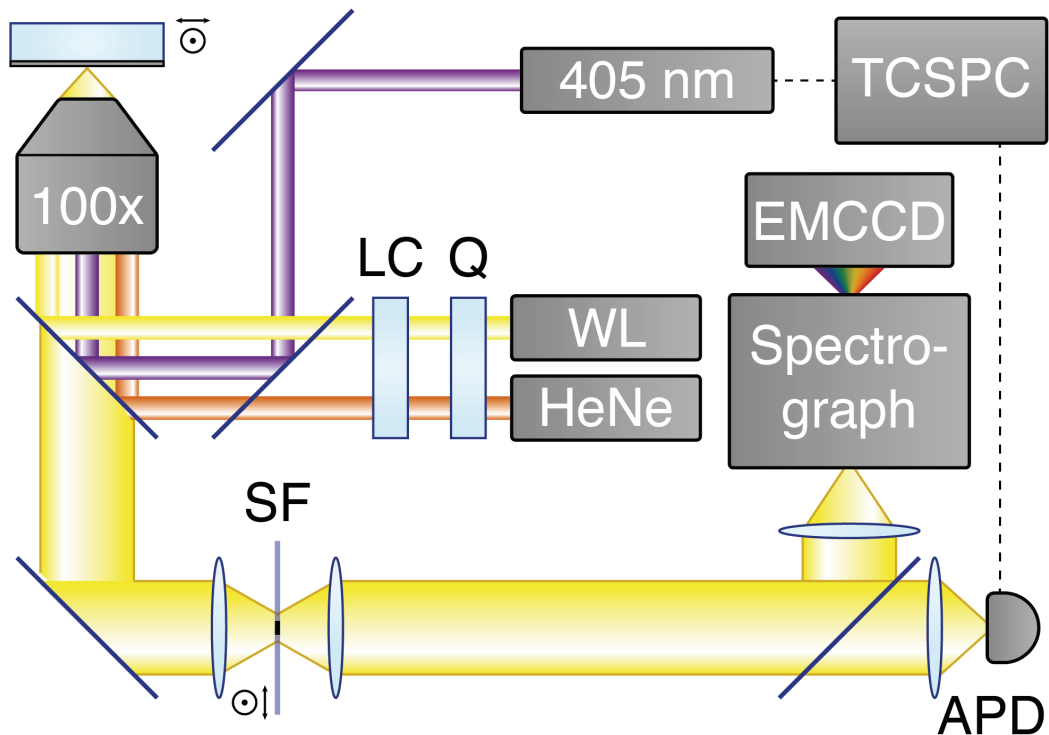


Figure S2. The experimental setup used to characterize the plasmon modes of the elliptical resonator and the energy-transfer process between quantum dots. The sample is imaged with a $100\times$ air objective on an inverted microscope. To launch SPPs, we direct a single-mode HeNe laser or a super-continuum white-light (WL) laser through a dichroic beam splitter to the objective. A Q-plate converts linear polarization into radial polarization and a liquid crystal variable retarder (LC) is used to correct for bi-refringence in the setup. To excite QDs, a 405-nm laser diode is used. Emission from the sample is collected on an imaging spectrograph with an EMCCD camera. A circular spatial filter (SF), placed in an intermediate image plane, is used to block the strong reflection of the laser spot. For time-resolved measurements, the emission is focused onto an avalanche photodiode (APD) connected to a time-correlated single-photon counting device (TCSPC).

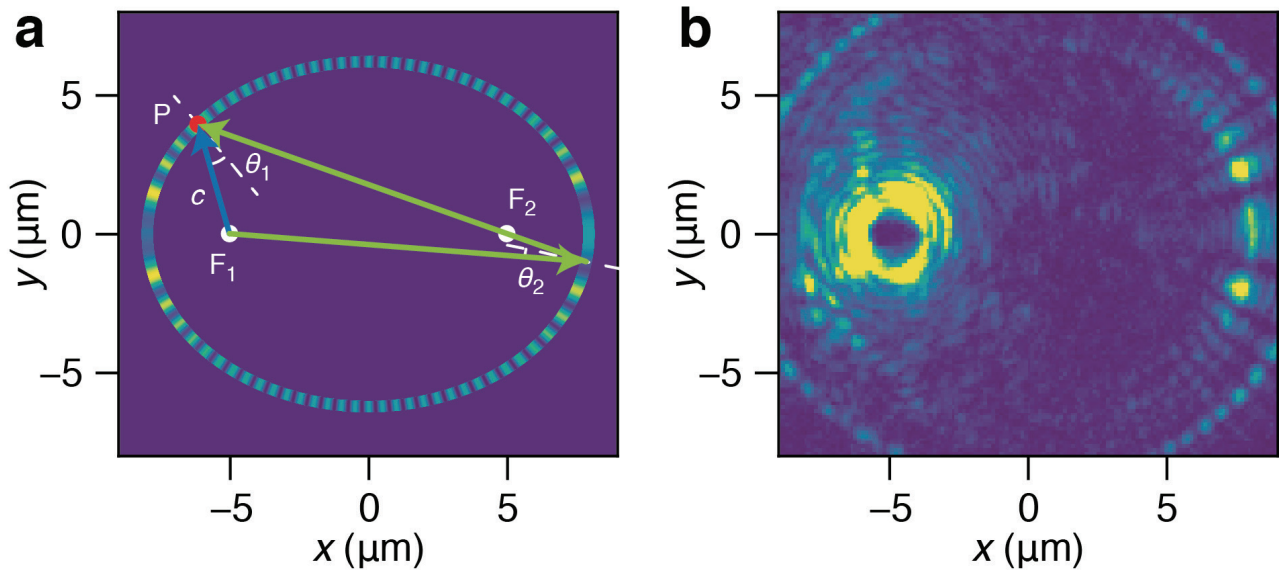


Figure S3. Interference model for SPPs in elliptical resonators. (a) Surface plasmons arriving at the reflector along the direct path (blue) and after one reflection (green) interfere to yield a calculated intensity profile along the reflector. (b) Experimental intensity profile of scattering SPPs along the elliptical reflector excited with the HeNe laser source (same data as Figure 2c in the main text).

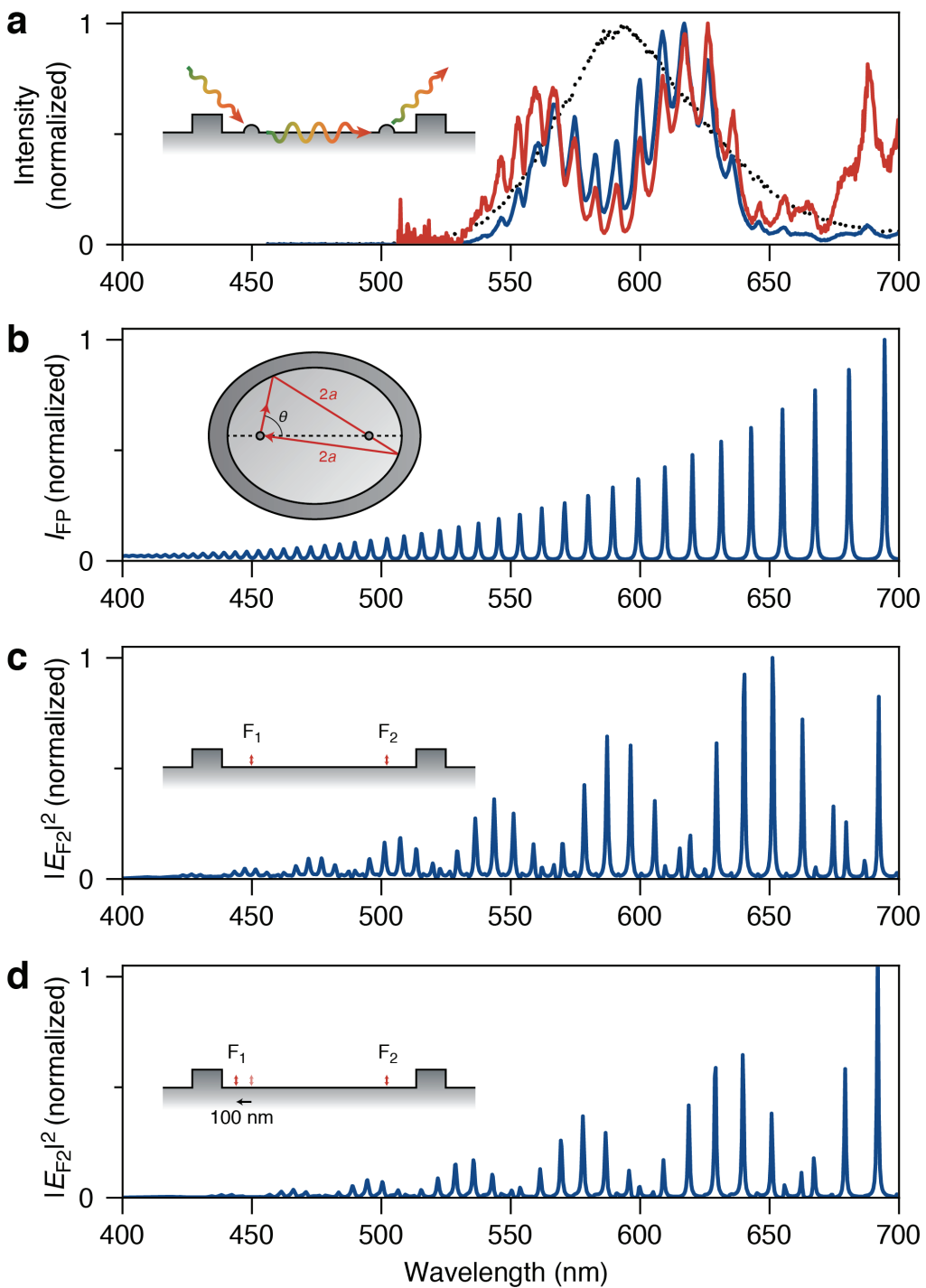


Figure S4. Transmission spectrum of a plasmonic ellipse. The blue line shows the transmission spectrum measured with a broadband super-continuum laser source (same data as in Figure 2a of the main text). The red line shows the transmission spectrum when normalized to the measured spectrum of the super-continuum source (black dotted line). (b) Ellipse resonances calculated with the Fabry–Pérot model. (c) Transmission spectrum from F₁ to F₂ calculated with numerical finite-element simulations in the frequency domain. (d) Simulated transmission spectrum when the dipole at F₁ is moved 100 nm away from the focal point.

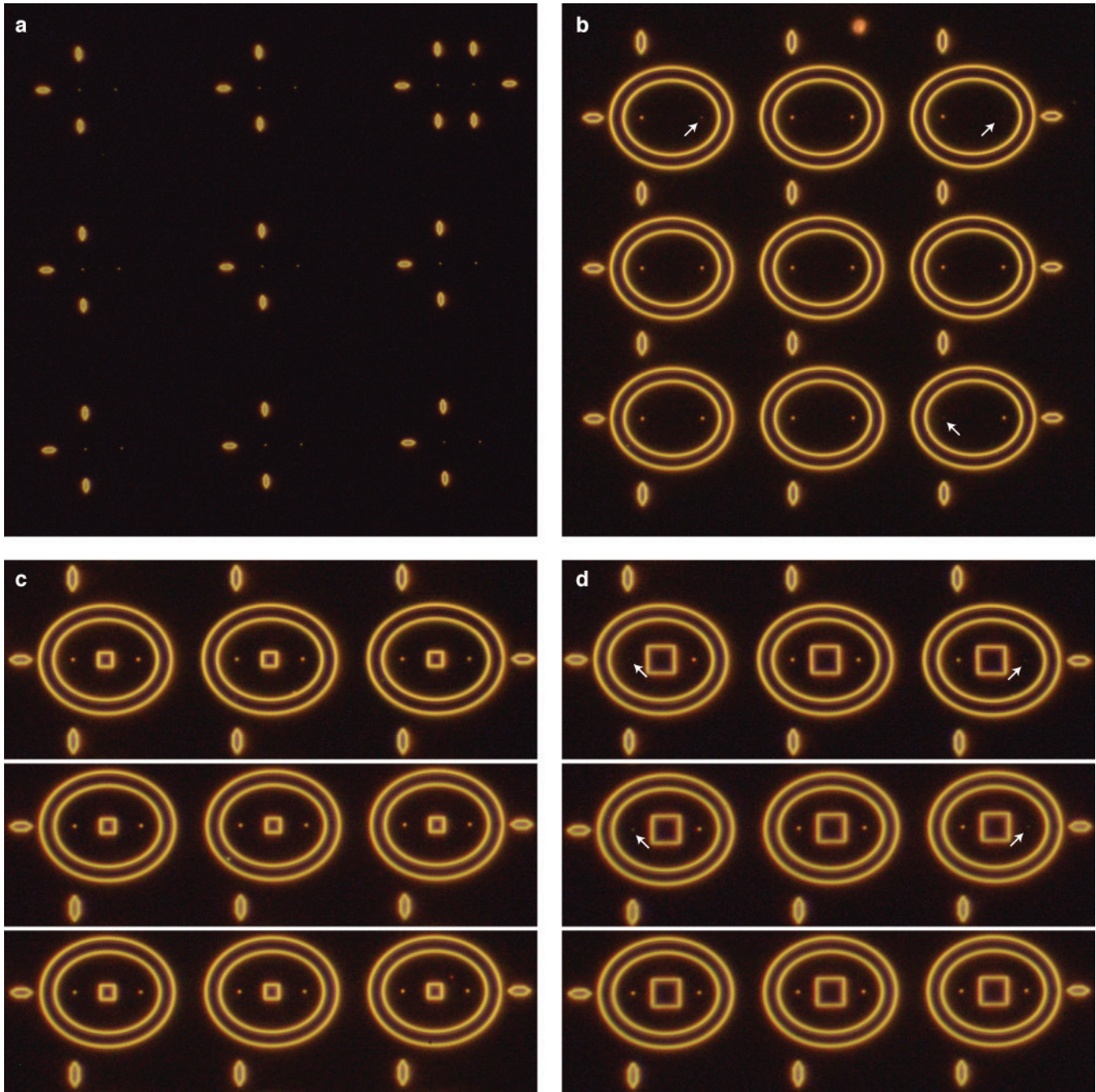


Figure S5. Dark-field microscopy images of the structures used for the statistics in Figure 3c of the main text. In each case, 9 different but nominally identical structures were fabricated on the same sample with (a) no elliptical reflector, (b) with an elliptical reflector, (c) with a $d = 2 \mu\text{m}$ defect, (d) with a $d = 4 \mu\text{m}$ defect. The structures with a missing Ag disk at one of the focal points, indicated by a white arrow, were rejected from the statistics.

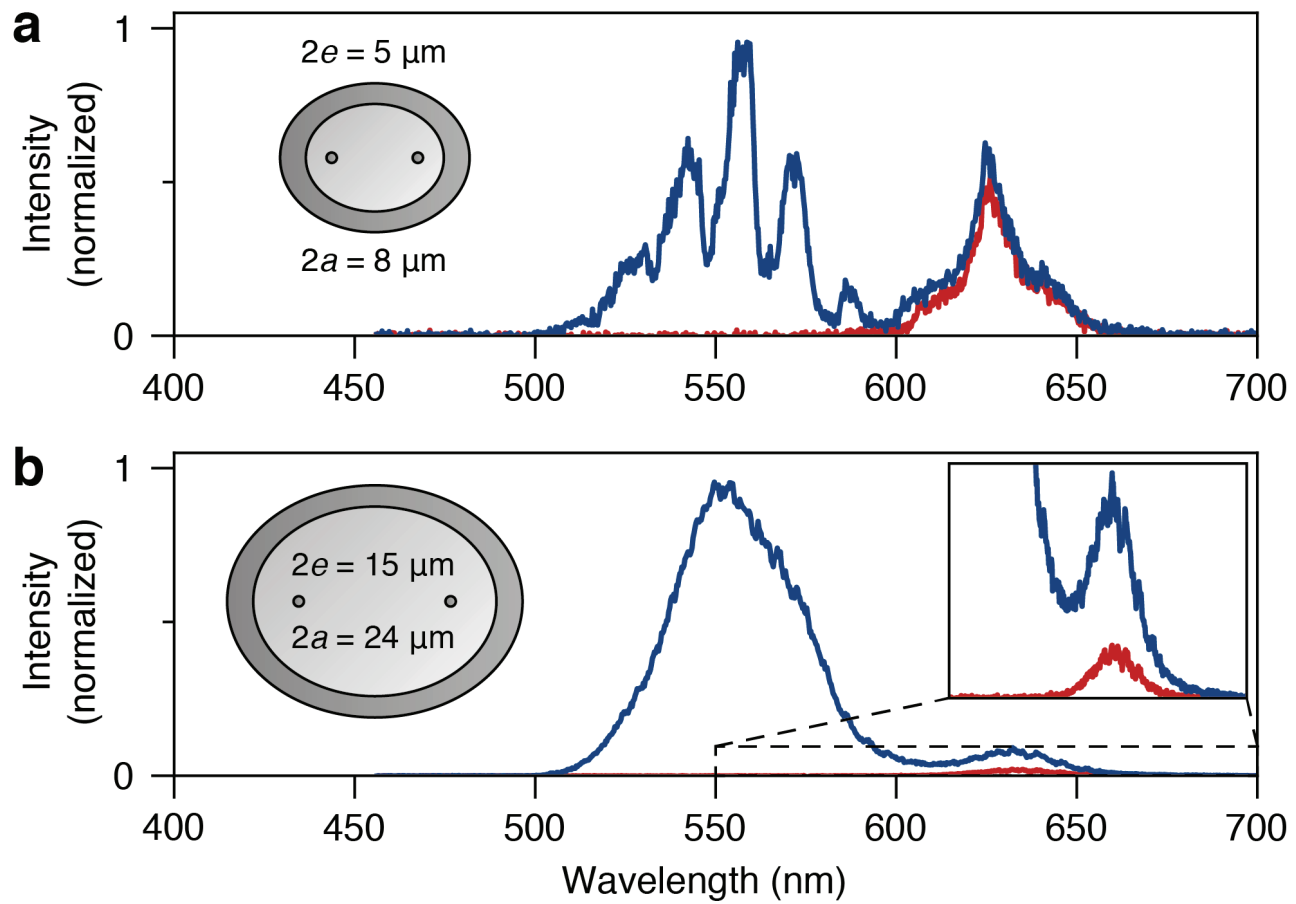


Figure S6. Photon intensity measured at the acceptor when the donor is excited with a focused laser spot before (blue line) and after (red line) permanently photobleaching the green donor QDs. (a) and (b) show the spectra for $2e = 5 \mu\text{m}$, $2a = 8 \mu\text{m}$ and $2e = 15 \mu\text{m}$, $2a = 24 \mu\text{m}$ ellipses, respectively. The inset in (b) emphasizes the difference in red emission before and after photobleaching the green QDs.

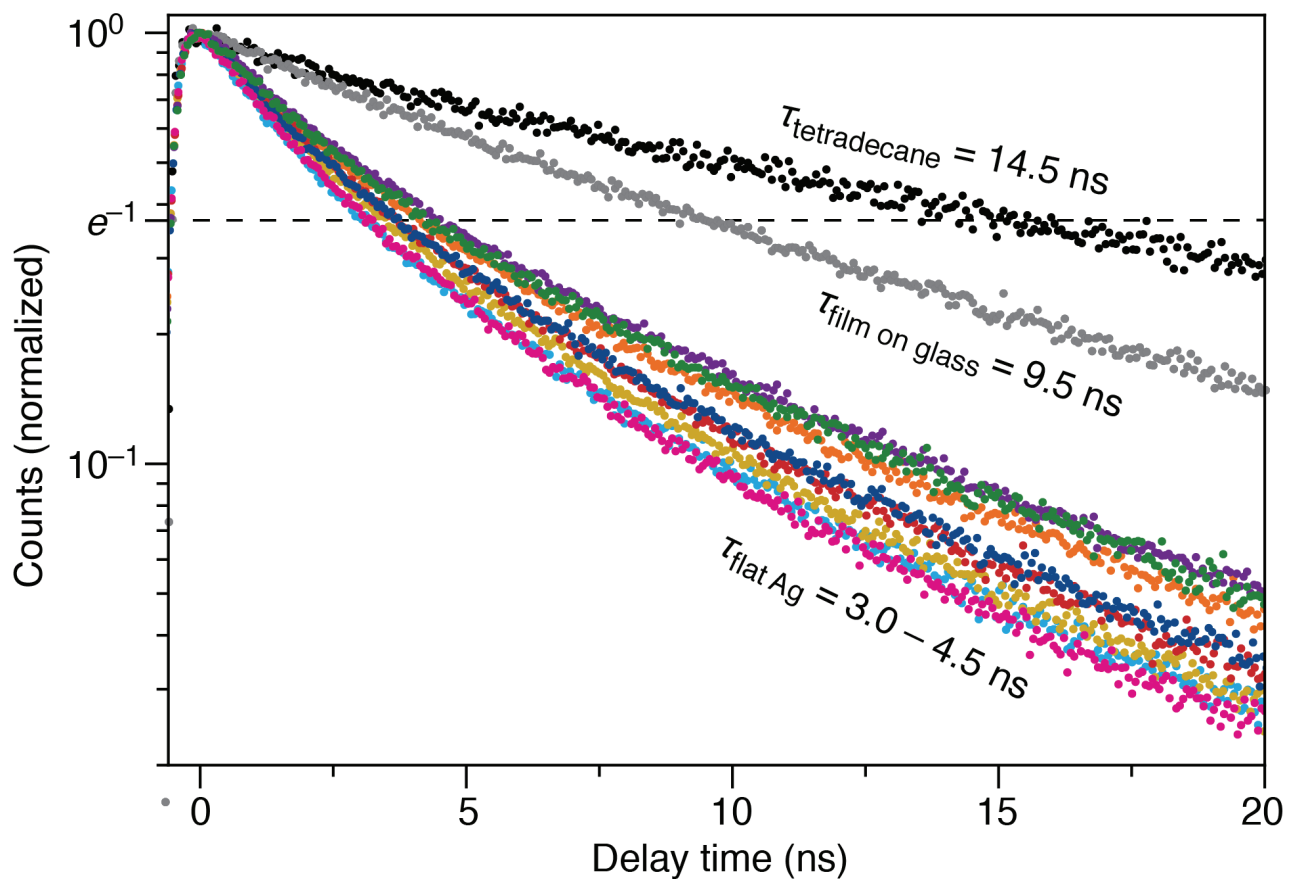


Figure S7. Time-resolved photoluminescence lifetime traces for donor quantum dots (QDs) in different environments (dispersed in tetradecane, as a film on glass, and printed as small ensembles on Ag). Colloidal QDs dispersed in tetradecane (black data) show a single-exponential decay with a 1/e lifetime of 14.5 ns. When the QDs are drop-cast on glass (gray data) the lifetime is reduced to 9.5 ns. This can be understood in terms of self-quenching when QDs are closely packed. When the QDs are printed in small ensembles on a flat Ag surface without an elliptical resonator (colored data) an additional acceleration of the decay occurs, presumably due to near-field coupling of the QDs to SPP modes. The lifetimes measured from eight different, but nominally identical, donor QD ensembles varies from $\sim 3.0 - 4.5$ ns. We ascribe this to random variations in the ensemble size, shape, and internal structure that are an unavoidable result of our printing procedure.

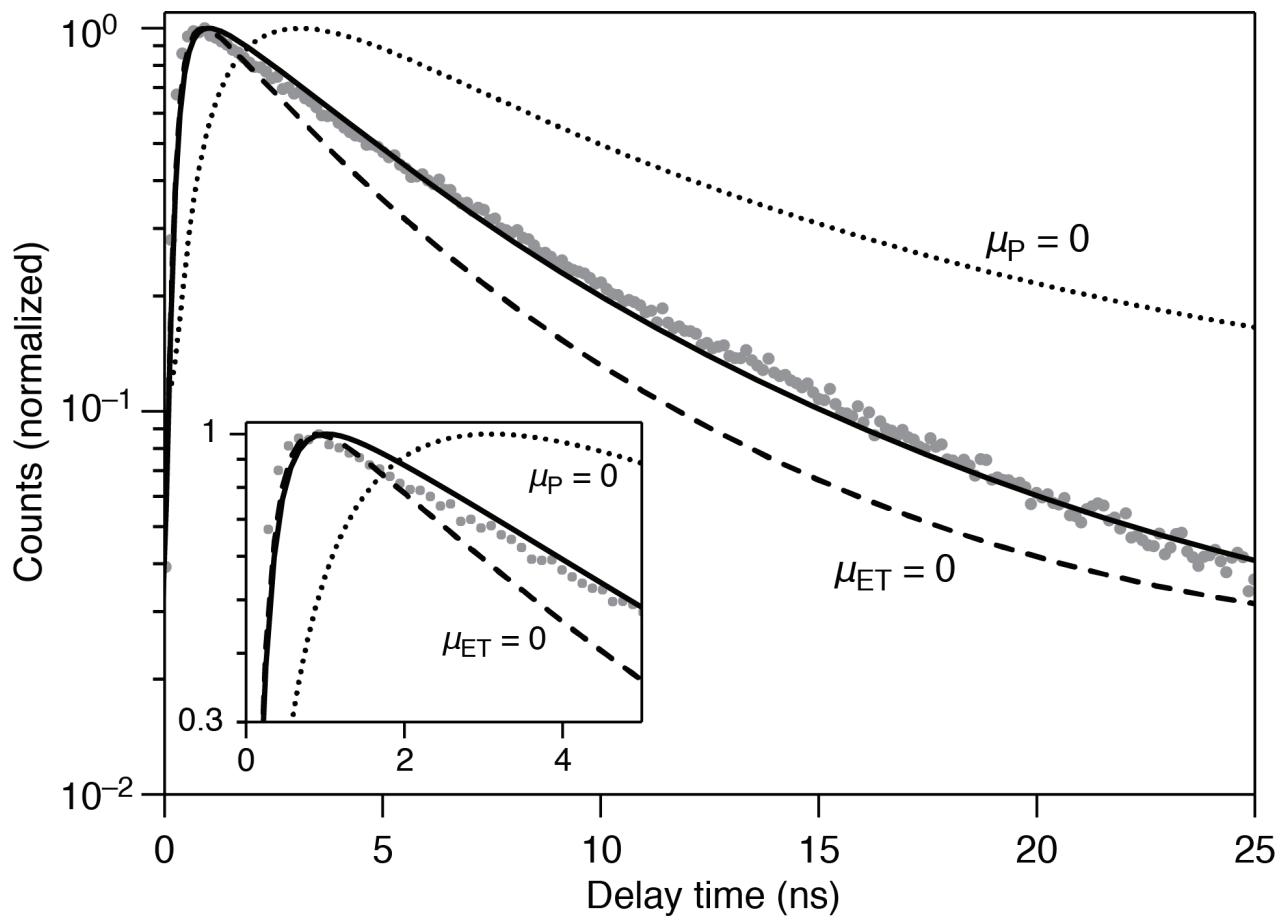


Figure S8. Fit of the rate-equation model (solid line) to the data (gray points) from Figure 4f in the main text. See section S3 above for details. The dotted line shows the result of the model (eq. S7–11) with no direct 405-nm plasmon excitation ($\mu_P = 0$) and the dashed line shows the result without contribution from energy transfer ($\mu_{ET} = 0$). The inset provides a magnified view of the dynamics for delay times up to 5 ns.

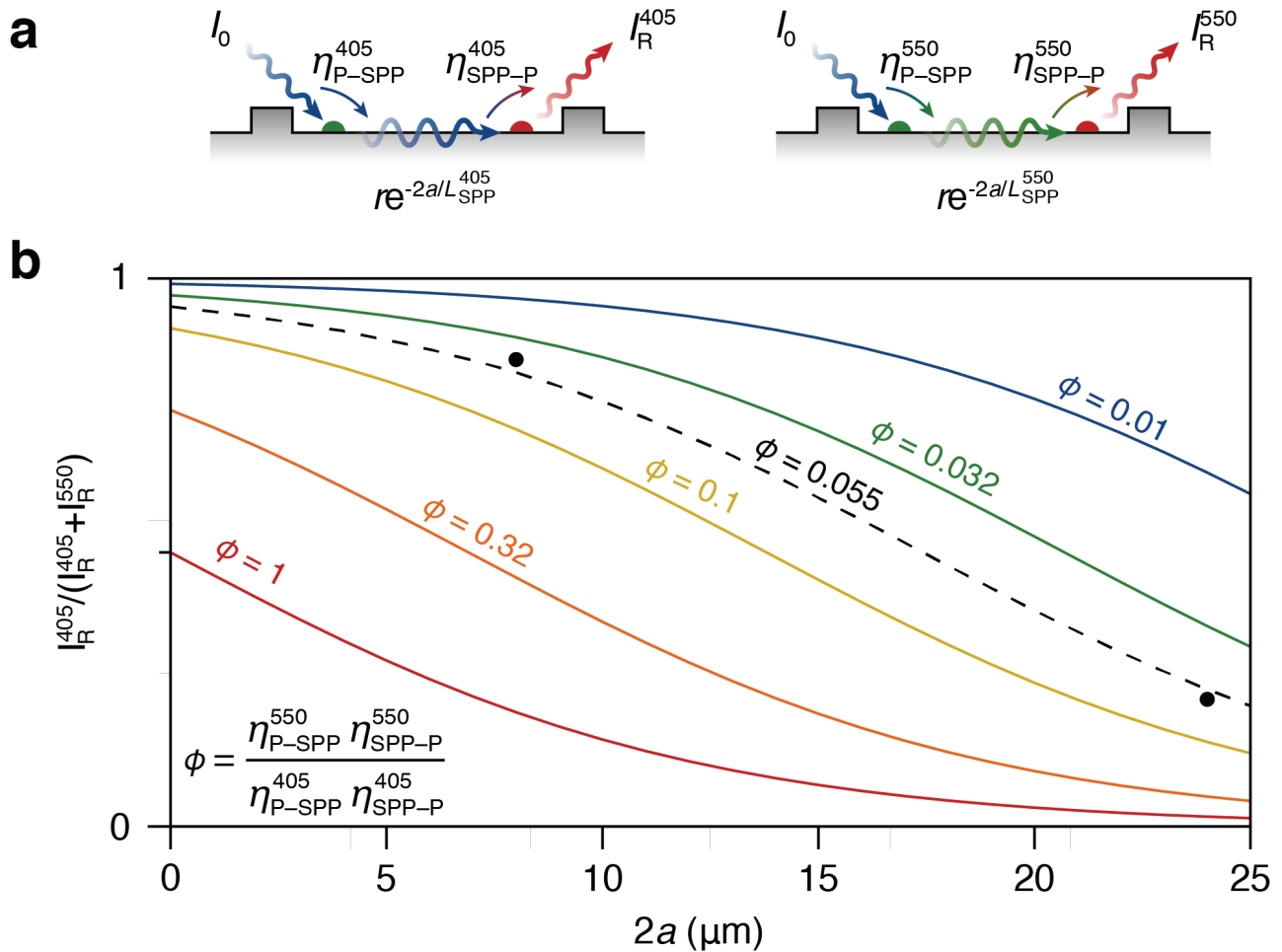


Figure S9. Fraction of the red acceptor photoluminescence resulting from excitation through 405-nm plasmons. (a) Schematic illustrating the red emission intensity I_R^{405} and I_R^{550} of the acceptor due to in-scattering of blue SPPs at the donor QDs (left) or emission of green SPPs (right), respectively. (b) Fraction of the red acceptor photoluminescence resulting from excitation through 405-nm SPPs, I_R^{405} , plotted as a function of twice the long half axis ($2a$) of the ellipse. The different lines represent various values of ϕ describing the ratio of photon–SPP coupling strengths, mediated by the QDs, at 405 and 550 nm. The black circles are the experimentally obtained data points of the ellipses depicted in Figure S6, and the dashed line is a fit of the model to the data.